
Ionization Waves of Arbitrary Velocity

Efforts to engineer plasmas for the generation and manipulation of electromagnetic waves have been growing in sophistication. Recent examples of plasma-based photonic devices include mirrors,¹ wave plates,^{2,3} polarizers,^{4,5} *q*-plates,⁶ radiation sources ranging from x rays^{7,8} to THz,^{9,10} laser amplifiers,^{11–13} and laser compressors.¹⁴ Many such tools rely on the controlled propagation of an ionization front, the velocity of which can strongly impact the performance of the system.

For example, a light source propagating within an ionization front will undergo “photon acceleration”—a continual upshift of its frequency induced by the dynamic refractive index gradient.^{15–18} However, the frequency upshift results in group velocity acceleration and a tendency for the source to decouple from the constant velocity ionization front. To highlight a second example, recent simulations of plasma-based laser amplification showed that a dynamic ionization front propagating just ahead of an amplifying seed pulse provides enhanced control over plasma parameters as well as improved noise suppression.¹⁹

A technique providing unprecedented spatiotemporal control over the propagation of laser intensity—the “flying focus”—was recently pioneered.^{20,21} A chirped broadband laser pulse with duration τ (with the sign of τ indicating the direction of the chirp) is focused by a highly chromatic diffractive optic that produces an extended focal region with length l . In general, each color reaches best focus at a unique time, and the rate at which the location of best focus moves is uniquely determined by the ratio τ/l for a linearly chirped beam. Peak laser intensity can be made to propagate at any velocity, from $-\infty$ to $+\infty$, by tuning τ/l .

Subsequent calculations have demonstrated that a dynamic ionization front will track the velocity of an intensity isosurface at the ionization threshold of a background gas.²² Therefore, the flying focus can be used to produce an ionization wave of arbitrary velocity (IWAV). These simulations also revealed that backward IWAV propagation relative to the ionizing laser mitigates ionization-induced refraction, which typically degrades the formation of long, uniform laser-produced plasmas.^{23,24}

In this article, we report the first experimental demonstration of ionization waves of arbitrary velocity. The velocities ranged from subluminal to superluminal (slower and faster than the speed of light, respectively), both forward- and backward-propagating relative to the ionizing laser. Ionization fronts were observed to propagate smoothly over several millimeters in most cases, although subluminal forward propagation was degraded by ionization-induced refraction, as expected. To diagnose the IWAV propagation, a novel spectrally resolved schlieren diagnostic was developed, exploiting the linear time–frequency relationship of a chirped probe. These data demonstrate the feasibility of flying-focus-produced IWAV’s for use in applications like those discussed above.

The experimental setup is shown in Fig. 154.17. An Nd:YLF laser with optical parametric chirped-pulse amplification (OPCPA) generated a beam with central wavelength $\lambda_0 = 1.053 \mu\text{m}$ and full-width-at-half-maximum (FWHM) bandwidth $\Delta\lambda = 8.7 \text{ nm}$, providing the source for the pump and probe beams. The linearly chirped pulse duration was tuned by adjusting the grating position in the stretcher. A beam splitter directed 85% of the energy to the pump path. A diffractive lens with radially varying groove density, described more fully in Ref. 21, was used to focus the pump beam in ambient air. Its focal length for the central wavelength of the pump was $f_0 = 51.1 \text{ cm}$, and it produced an extended focal region of length $l = f_0\Delta\lambda/\lambda_0 = 4.2 \text{ mm}$, with the red and blue sides of the spectrum focusing nearest to and farthest from the lens, respectively. With an energy of $25.5 \pm 0.3 \text{ mJ}$, the pump could create a plasma channel in air at best focus for pulse durations ranging from best compression ($<1 \text{ ps}$) up to $\approx 40 \text{ ps}$.

The additional 15% transmitted through the beam splitter was down-collimated, converted to 2ω using a second-harmonic crystal, and directed to the plasma orthogonal to the pump axis for use as a probe beam. An optical delay path was used to time the probe such that its passage coincided with the IWAV propagation. The plasma channel was imaged along the probe path onto the entrance slit of a 0.3-m imaging spectrometer equipped with a 1200-grooves/mm grating. A

knife edge was used as a schlieren stop in a focal location of the probe beam along the imaging path. It was oriented in order to probe gradients orthogonal to the axis of the plasma

channel (i.e., the edge of the channel). A Finger Lakes charge-coupled-device (CCD) camera was used to capture images at the exit plane of the spectrometer.

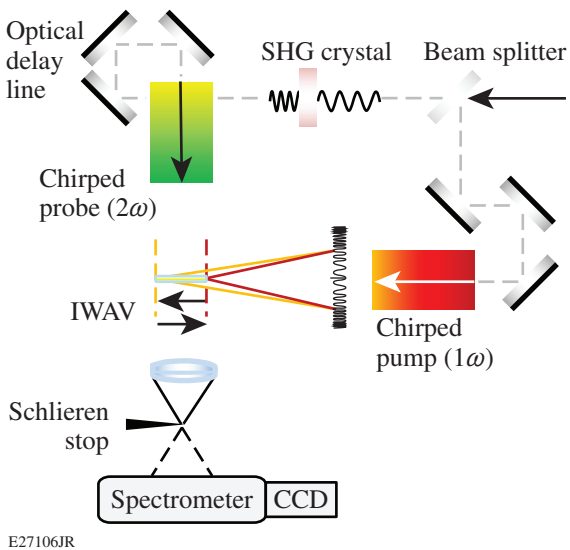


Figure 154.17

Experimental setup: a $1.053\text{-}\mu\text{m}$ laser with tunable pulse duration τ was split into two beams. The pump beam remained 1ω and was focused by a diffractive optic to produce an ionization wave of arbitrary velocity (IWAV). The probe beam was converted to 2ω and diagnosed the plasma channel in a side-on geometry coincident with the plasma formation. A spectrally resolved schlieren diagnostic was used to determine the ionization front velocity. SHG: second-harmonic generation; CCD: charge-coupled device.

Removing the schlieren stop, opening the spectrometer slit, and operating the spectrometer in zero order, the CCD camera captured a 2-D shadowgraphy image of the plasma channel. Inserting the schlieren stop with otherwise the same parameters yielded a 2-D schlieren image. The spectrometer slit was then centered on the edge of the plasma channel (the location of maximum signal) and the grating was set to disperse the probe wavelengths orthogonal to the plasma channel axis. The spectral axis effectively provides picosecond time resolution as a result of the linear time-frequency dependence of the chirped probe beam.

Figure 154.18(a) shows the flying focus focal-spot velocity (expected to correspond directly to the ionization front velocity) given by $v_f = dz/dt = c(1 + \tau c/l)^{-1}$ (Ref. 21). Negative values of the pulse duration τ correspond to negatively chirped beams, with the blue end of the spectrum preceding the red end in time. The IWAV velocity is converted to an observable on the spectrally resolved schlieren measurement by noting that $dz/dt = (dz/d\lambda)(d\lambda/dt)$, and for the linearly chirped second-harmonic probe beam, the derivative $d\lambda/dt = -\Delta\lambda/2\tau$ (i.e., the FWHM spectral bandwidth of the probe—half that of the pump—is spread out over the FWHM pulse duration). Therefore, the expected edge slope on the schlieren diagnostic is given by

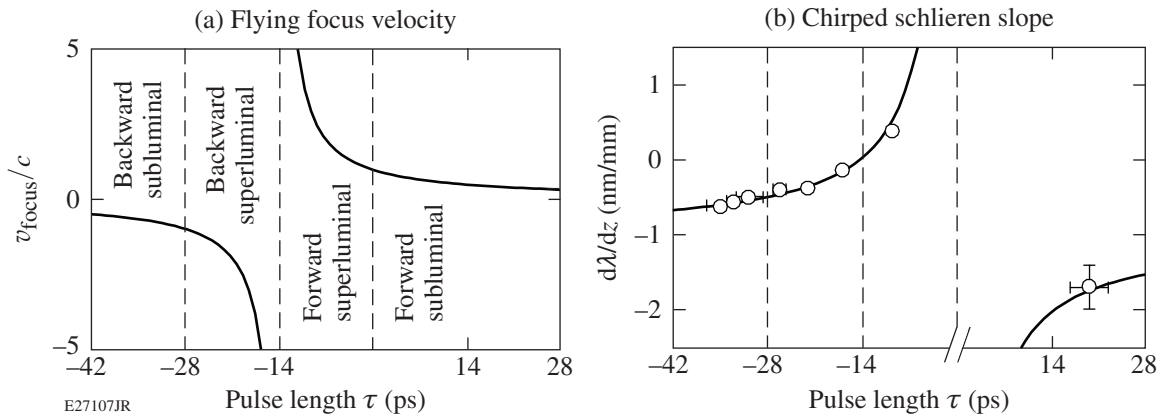


Figure 154.18

(a) The flying focus velocity (i.e., the speed at which constant intensity isosurfaces move near best focus) is determined by the ratio of the chirped-pulse duration to the length of the extended chromatic focal region produced by the diffractive optic. Any velocity (including faster than the speed of light) is achievable in both the forward and backward directions relative to the laser propagation. (b) For the spectrally resolved schlieren diagnostic, the expected linear slope of an edge marking the onset of plasma formation is plotted as a function of pump and probe pulse duration. The overlaid points correspond to the experimental data. Both forward- and backward-propagating ionization waves of arbitrary velocity were produced, with velocities both less than and greater than the speed of light in each direction.

$d\lambda/dt = -\Delta\lambda/2 [(1/c\tau) + (1/l)]$; this slope is plotted as a function of pulse length in Fig. 154.18(b).

Results from the spectrally resolved schlieren diagnostic are shown in Fig. 154.19. Each image is an average of five to ten shots divided by an average of several reference spectra, which were obtained by removing the schlieren stop and blocking the pump beam. The pump beam propagated from left to right along the z axis. An edge-finding routine was used to find the time of the ionization wave's appearance at each axial location; vertical lineouts were taken averaging over $\approx 30\text{-}\mu\text{m}$ increments along the z axis, and typically the value closest to 10% along the spectral axis was specified as the edge. The slope was determined from a linear best fit through the data points. The points found by the edge-finding routine, as well as the best fit result, are plotted with the data in Fig. 154.19.

In Figs. 154.19(a)–154.19(c), there is no signal on the blue side of the probe spectrum because that portion of the probe passed the pump's focal region prior to any plasma formation. The edge of the signal then appears and varies linearly, as expected, over a distance of at least 2 to 3 mm. Hydrodynamic expansion of the plasma channel is negligible on the time scale of the probe beam, so the plasma channel persists and continues

to refract all subsequent probe colors on the red side of the spectrum. Figures 154.19(a) and 154.19(b) are both examples of superluminal backward propagation since $-2l/c < \tau < -l/c$; the latter example is close to $t = -l/c$, in which case each color arrives at best focus simultaneously and the IWAV travels across the focal region instantaneously.

Figure 154.19(c) shows an example of superluminal forward propagation, with $-l/c < \tau < 0$. Note that although the IWAV co-propagates with the ionizing laser, ionization-induced refraction did not compromise the channel formation. This naturally follows from the fact that the shorter-wavelength photons that ionize the plasma at larger values along the z axis are ahead of the ionization front and are therefore not affected by propagation through the existing plasma. (Similar logic explains why superluminal IWAV propagation does not violate causality.)

In Fig. 154.19(d), the laser is positively chirped, which always yields a subluminal forward-propagating flying focus. Note that the sign of the slope expected in the schlieren images is the same as for negatively chirped backward propagation because two sign changes (the IWAV propagation direction and the direction of the probe chirp) cancel one another out; only within the narrow range $-l/c < \tau < 0$ is the slope positive

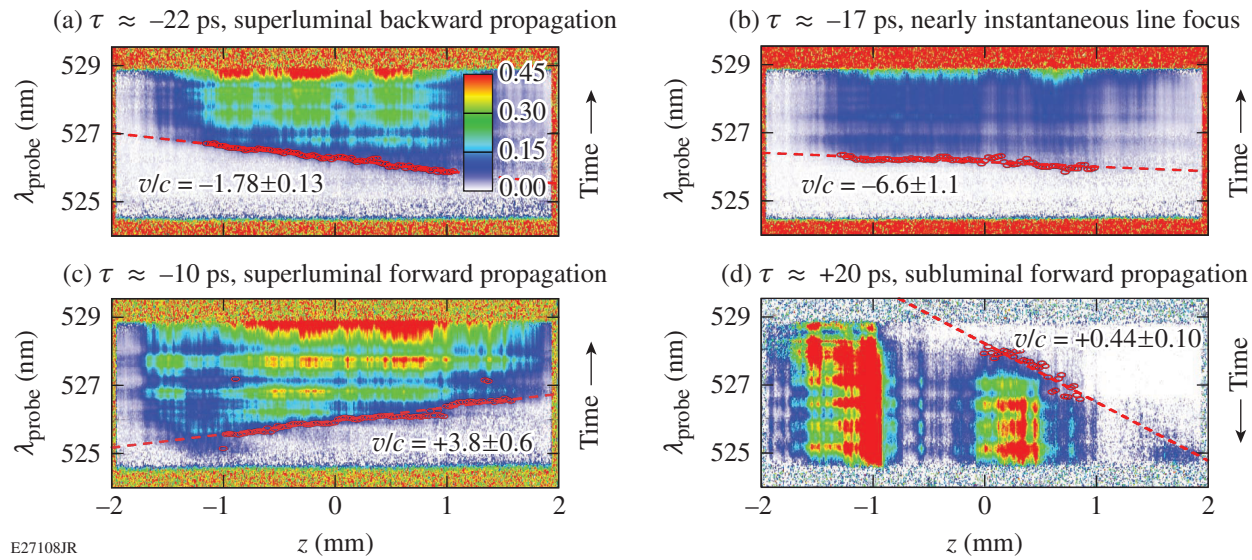


Figure 154.19

Spectrally resolved schlieren results. (a) An example of superluminal backward propagation for $\tau \approx -22$ ps. The probe is negatively chirped so the direction of time is from the blue end to the red end of the spectrum. The IWAV begins at $+z$ and propagates backward to $-z$ along the pump axis. (b) A more highly superluminal example producing a nearly instantaneous line focus. (c) With $-l/c < \tau < 0$, the IWAV remains superluminal but switches to forward-propagating, reversing the sign of the slope. (d) When the probe is positively chirped, the direction of time is effectively reversed, and subluminal forward propagation produces a disjointed plasma channel because of ionization-induced refraction.

because the IWAV's are forward-propagating but the probe chirp is negative [e.g., Fig. 154.19(c)]. The reversed direction of time is evident in the schlieren image because the blue side of the spectrum probes the fully formed plasma channels in contrast to the previous examples. Note also that for $\tau > -l/(2c)$, the time v_f/l that it takes the IWAV to propagate from one edge of the focal region to the other is greater than the probe pulse duration $|\tau|$, limiting the IWAV propagation distance that the probe can diagnose. Therefore, in the example shown, the plasma is already over 1 mm in length by the time the probe arrives.

The key difference in Fig. 154.19(d) is that the schlieren signal appears disjointed along the axis of the pump beam. This results from ionization-induced refraction in the case of sub-luminal forward propagation—an effect that was predicted in Ref. 22. To illustrate this more clearly, 2-D shadowgraphs and 2-D schlieren images are shown for three cases in Fig. 154.20. The example in Fig. 154.20(a) happens to be the case of a nearly instantaneous line focus, but all cases of backward propagation that were tested, in addition to superluminal forward propagation, produced similar long, uniform plasma channels. Contrast that with Fig. 154.20(b), which shows that the initial plasma at $z = -1$ mm disrupts subsequent plasma formation over the

next ≈ 1 mm. At a later point along the pump axis, the initial plasma is far enough away (refracting a small enough fraction of the wavelength that focuses to that location) that ionization is once again triggered locally. This cycle repeats itself once more, producing three distinct sparks [the third being more evident in Fig. 154.19(d) than in Fig. 154.20(b)].

Using the edge-finding routine on the middle spark resulted in a linear fit that roughly tracks the central plasma and also seems to predict the timing of the third plasma's formation, but the fit's confidence was much lower, resulting in larger error bars. The slopes for all data sets, including subluminal backward propagation (which has not been shown), were overplotted with the analytic calculation in Fig. 154.18(b). In most cases, the uncertainties in pulse length and schlieren slope were smaller than the marker size shown, with the exception of the sub-luminal forward-propagating IWAV just described; nevertheless, that result is also in good agreement with the prediction.

For completeness, Fig. 154.20(c) shows the plasma channel formation that occurs when the probe duration was at best compression ($\tau \approx 500$ fs). In this case, the diffractive lens produces a distributed focal spot that would be expected to have approximately constant intensity over several millimeters

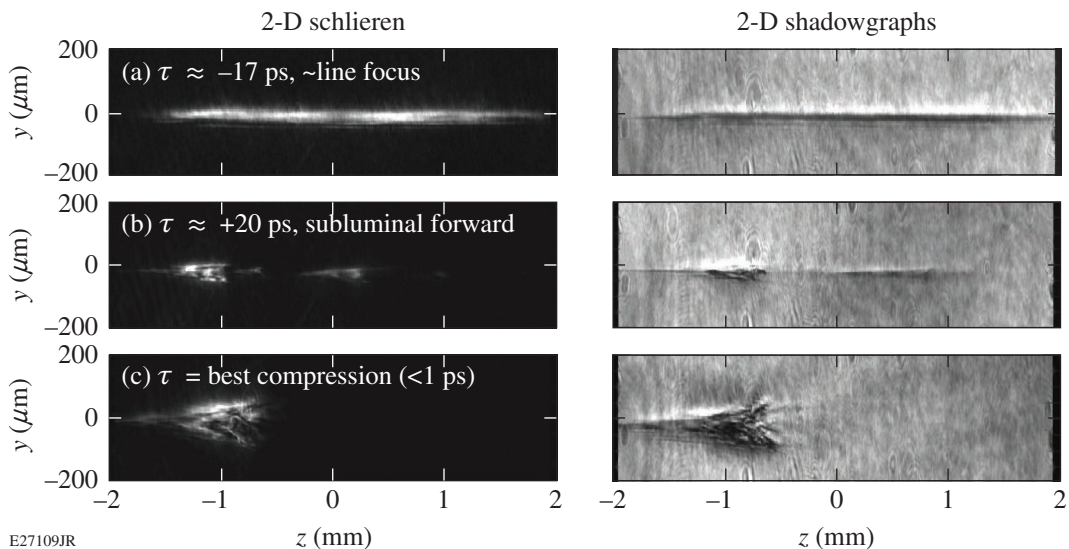


Figure 154.20

Two-dimensional schlieren and shadowgraphy of various cases. (a) The $\tau \approx -17$ -ps example shows a long, uniform plasma channel and is representative of all tested cases of backward propagation as well as superluminal forward propagation. (b) Subluminal forward propagation leads to plasma channel breakup because of ionization-induced refraction; (c) this also occurs for best compression, which is most similar to conventional beam propagation in that laser intensity moves forward at the group velocity.

while propagating at the laser's group velocity (and is therefore the case most similar to conventional beam propagation). This case was degraded even more severely by ionization-induced refraction such that only one short plasma was formed.

In summary, ionization waves of arbitrary velocity have been demonstrated experimentally using the flying focus. While superluminal ionization front propagation has been demonstrated previously,²⁵ and a different (more complicated) scheme for tuning the velocity of ionization waves has been proposed,²⁶ to our knowledge this represents the first experimental demonstration of IWAV's. Producing plasma channels in this manner could facilitate improved performance in a wide range of applications that rely on synchronization with an ionization front, such as plasma-based laser amplification, photon acceleration, and THz generation. Even neglecting the potentially beneficial dynamics of the ionization front, we have demonstrated long, uniform, flying focus-produced plasma channels that are comparable to those created using an axicon lens, which may be of interest to applications that utilize plasma waveguides.^{27–30}

ACKNOWLEDGMENT

This work was supported by the U.S. Department of Energy Office of Fusion Energy Sciences under contract No. DE-SC0016253, Department of Energy under Cooperative Agreement No. DE-NA0001944, the University of Rochester, and the New York State Energy Research and Development Authority. The support of DOE does not constitute an endorsement by DOE of the views expressed in this article.

REFERENCES

1. C. Thaury *et al.*, Nat. Phys. **3**, 424 (2007).
2. P. Michel *et al.*, Phys. Rev. Lett. **113**, 205001 (2014).
3. D. Turnbull, P. Michel, T. Chapman, E. Tubman, B. B Pollock, C. Y Chen, C. Goyon, J. S Ross, L. Divol, N. Woolsey, and J. D Moody, Phys. Rev. Lett. **116**, 205001 (2016).
4. D. J. Stark *et al.*, Phys. Rev. Lett. **115**, 025002 (2015).
5. D. Turnbull, C. Goyon, G. E. Kemp, B. B. Pollock, D. Mariscal, L. Divol, J. S. Ross, S. Patankar, J. D. Moody, and P. Michel, Phys. Rev. Lett. **118**, 015001 (2017).
6. K. Qu, Q. Jia, and N. J. Fisch, Phys. Rev. E **96**, 053207 (2017).
7. M. R. Edwards and J. M. Mikhailova, Phys. Rev. Lett. **117**, 125001 (2016).
8. M. R. Edwards, J. M. Mikhailova, and N. J. Fisch, Phys. Rev. E **96**, 023209 (2017).
9. C. D'Amico *et al.*, Phys. Rev. Lett. **98**, 235002 (2007).
10. K. Y. Kim *et al.*, Opt. Express **15**, 4577 (2007).
11. G. Shvets *et al.*, Phys. Rev. Lett. **81**, 4879 (1998).
12. L. Lancia *et al.*, Phys. Rev. Lett. **116**, 075001 (2016).
13. R. K. Kirkwood, D. P. Turnbull, T. Chapman, S. C. Wilks, M. D. Rosen, R. A. London, L. A. Pickworth, W. H. Dunlop, J. D. Moody, D. J. Strozzi, P. A. Michel, L. Divol, O. L. Landen, B. J. MacGowan, B. M. Van Wonterghem, K. B. Fournier, and B. E. Blue, Nat. Phys. **14**, 80 (2018).
14. V. M. Malkin, G. Shvets, and N. J. Fisch, Phys. Rev. Lett. **82**, 4448 (1999).
15. W. B. Mori, Phys. Rev. A **44**, 5118 (1991).
16. E. Esarey, G. Joyce, and P. Sprangle, Phys. Rev. A **44**, 3908 (1991).
17. P. Sprangle and E. Esarey, Phys. Fluids B **4**, 2241 (1992).
18. J. M. Dias *et al.*, Phys. Rev. Lett. **78**, 4773 (1997).
19. D. Turnbull, S. Bucht, A. Davies, D. Haberberger, T. Kessler, J. L. Shaw, and D. H. Froula, Phys. Rev. Lett. **120**, 024801 (2018).
20. A. Sainte-Marie, O. Gobert, and F. Quéré, Optica **4**, 1298 (2017).
21. D. H. Froula, D. Turnbull, A. S. Davies, T. J. Kessler, D. Haberberger, J. P. Palastro, S.-W. Bahk, I. A. Begishev, R. Boni, S. Bucht, J. Katz, and J. L. Shaw, "Spatiotemporal Control of Laser Intensity," to be published in Nature Photonics.
22. J. P. Palastro, D. Turnbull, S.-W. Bahk, R. K. Follett, J. L. Shaw, D. Haberberger, J. Bromage, and D. H. Froula, Phys. Rev. A **97**, 033835 (2018).
23. W. P. Leemans *et al.*, Phys. Rev. A **46**, 1091 (1992).
24. T. M. Antonsen, Jr. and Z. Bian, Phys. Rev. Lett. **82**, 3617 (1999).
25. I. Alexeev, K. Y. Kim, and H. M. Milchberg, Phys. Rev. Lett. **88**, 073901 (2002).
26. A. Zhidkov *et al.*, Phys. Rev. Lett. **103**, 215003 (2009).
27. C. G. Durfee and H. M. Milchberg, Phys. Rev. Lett. **71**, 2409 (1993).
28. P. Volfbeyn, E. Esarey, and W. P. Leemans, Phys. Plasmas **6**, 2269 (1999).
29. Y.-F. Xiao *et al.*, Phys. Plasmas **11**, L21 (2004).
30. S. Z. Green *et al.*, Plasma Phys. Control. Fusion **56**, 084011 (2014).